THE JOURNAL OF PHYSICAL CHEMISTRY LETTERS
A JOURNAL OF THE AMERICAN CHEMICAL SOCIETY

pubs.acs.org/JPCL

Letter

Theoretical Insight into Herzberg–Teller Spin–Vibronic Coupling Enhanced Reverse Intersystem Crossing in Hybrid MR-TADF Emitters

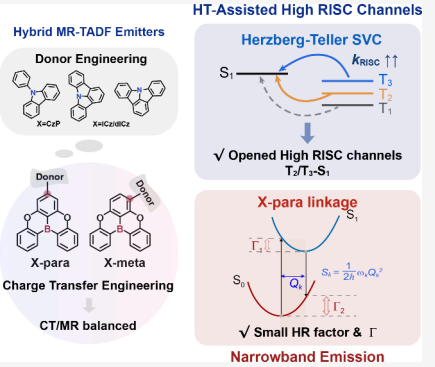
Yaxin Wang, Xiao Chen, Shanhao Deng, and Zhigang Shuai*

Cite This: *J. Phys. Chem. Lett.* 2026, 17, 11381–11390

Read Online

ACCESS | Metrics & More | Article Recommendations | Supporting Information

ABSTRACT: Hybrid multiple-resonance thermally activated delayed fluorescence (MR-TADF) emitters can combine narrowband emission with efficient triplet harvesting, but the factors governing these properties remain unclear. Here, we investigate 12 BO-acceptor MR-TADF emitters using quantum-chemical calculations and the thermal vibration correlation function formalism. Our results reveal distinct origins of color purity and reverse intersystem crossing (RISC) kinetics. High color purity is governed by the collective structural–vibronic response rather than charge-transfer character alone, with para-linkage favoring narrow emission through reduced overall vibronic reorganization. The equilibrium-limit effective RISC descriptor reflects channel-specific rates and higher-triplet thermal accessibility. For emitters with complete channel-resolved data, the fastest intrinsic RISC pathway consistently lies within the higher-triplet T_2/T_3 manifold, while Herzberg–Teller (HT) coupling selectively enhances specific higher-triplet channels relative to Franck–Condon values.

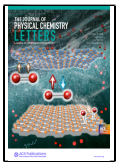


Organic light-emitting diodes (OLEDs) have emerged as promising candidates for next-generation ultrahigh-definition displays because of their exceptional flexibility, thin form factors, and vibrant color gamut.[1,2] The fundamental challenge in OLED material design lies in balancing two critical parameters: color purity, characterized by a narrow full width at half-maximum (fwhm), and emission efficiency, which critically depends on efficient harvesting of triplet excitons through reverse intersystem crossing (RISC).[3−5] Conventional thermally activated delayed fluorescence (TADF) emitters can realize unity internal quantum efficiency by harvesting triplet excitons via RISC, a process that relies on a small singlet–triplet energy gap (ΔE_{ST}).[6] Such a small ΔE_{ST} is typically achieved by constructing a donor–acceptor (D–A) architecture that spatially separates the frontier molecular orbitals, imparting long-range charge-transfer (LRCT) character to the emissive S_1 state.[7,8] However, this LRCT character, while enabling RISC, often results in broad emission spectra (fwhm >40 nm) owing to significant structural relaxation and strong vibronic coupling, thereby compromising color purity and limiting their application in ultrahigh-definition displays.[3,9−11]

To overcome this limitation, multiple-resonance TADF (MR-TADF) emitters have been developed, which typically incorporate alternating electron-donating and electron-accepting atoms within a rigid polycyclic framework.[12,13] This design generates opposite resonance effects that spatially separate the highest occupied and lowest unoccupied molecular orbitals (HOMO and LUMO) at the atomic scale, imparting short-range charge-transfer (SRCT) character to the emissive state while preserving structural rigidity.[12−14] As a result, the singlet–triplet energy gap (ΔE_{ST}) is minimized and vibronic broadening is suppressed, enabling narrowband emission with fwhm values below 30 nm and small Stokes shifts.[12−17] A variety of boron-based MR analogues, including B–O, B–S, and N–C=O frameworks, have been investigated to expand the structural scope of this class.[18−20] Despite these advances, the similar SRCT character of the lowest singlet (S_1) and triplet (T_1) states leads to weak spin–orbit coupling (SOC) and thus relatively slow RISC rates ($k_{RISC} \approx 10^3$–10^4 s^{-1}).[14,21−23] This slow triplet upconversion can give rise to pronounced efficiency roll-off at high current densities, limiting device operational lifetimes and constraining the practical application of MR-TADF emitters in high-performance OLEDs.[21,24,25]

To address the slow RISC rates that limit MR-TADF device performance, hybrid architectures have been actively explored, in which a rigid MR chromophore is coupled to a conventional donor or a second MR fragment to introduce additional charge-transfer character.[24,26−34] For instance, Zhu and co-workers linked two MR units via a conjugated linkage, opening a high-lying $T_6 \rightarrow S_1$ RISC channel and producing near-ultraviolet emission with a 28 nm bandwidth.[35] In contrast, Adachi and co-workers combined LRCT and SRCT character in C–C-linked multiple-resonance charge-transfer (MRCT)-

Received: August 4, 2026
Revised: September 18, 2026
Accepted: September 18, 2026
Published: September 23, 2026



ACS Publications © 2026 American Chemical Society

Downloaded from pubs.acs.org/jpclcd/article-pdf/17/40/11381/6861567/6/acs.jpclett.6c02618.pdf by CHINESE UNIV OF HONG KONG SHENZHEN user on 02 November 2026

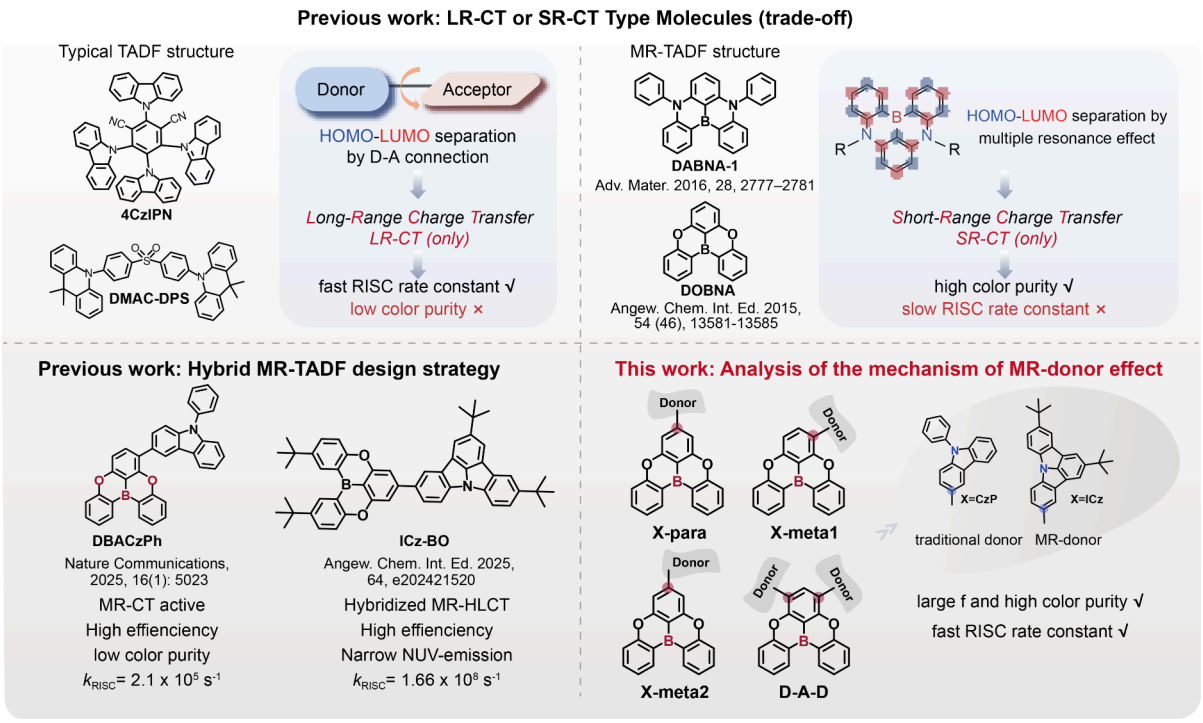


Figure 1. Schematic of the design strategy and molecular structures of the BO-acceptor-based hybrid MR-TADF emitters investigated in this work.

type D−A and D−A−D emitters, enabling a ^{3}MRCT → ^{3}LE → ^{1}MRCT upconversion pathway.[36] While both strategies have been shown to enhance k_{RISC}, the precise mechanistic differences between them—for example, in the manifold of triplet states that mediate RISC and the degree of SRCT/LRCT mixing—remain poorly understood.[23,35−41] This lack of clarity is particularly consequential as the molecular architecture grows in complexity, where traditional descriptors such as ΔE_{ST} or a single static S_1−T_1 spin−orbit coupling matrix element are often insufficient to capture the photophysical and kinetic consequences of hybridization.[42−47] Elucidating how donor identity, linkage topology, and nuclear motion collectively govern excited-state dynamics in these systems therefore represents an urgent need, motivating higher-level theoretical treatments and a systematic examination of the relevant structure−property relationships.[23,37,39,41]

To address these questions, we designed a series of 12 BO-acceptor-based hybrid MR-TADF emitters with systematically varied donor units and linkage topologies (Figure 1). The donors included CzP, a conventional TADF donor with strong LRCT character, and the rigid MR-type donors dICz and ICz, which maintain SRCT-dominated excited states. Each donor was connected to the BO acceptor via four distinct topologies: para, two inequivalent meta positions (meta1 and meta2), and D−A−D. This design allowed us to probe how connectivity modulates donor−acceptor electronic coupling and the resulting SRCT/LRCT balance, and to disentangle the roles of donor identity and linkage topology in dictating emission energy, spectral width, and RISC kinetics. By combining electronic-structure analysis, vibrationally resolved spectra from the thermal vibration correlation function formalism, and channel-resolved Franck−Condon and Herzberg−Teller (HT) rate calculations, we identified two distinct structure−property relationships. Donor identity and linkage topology primarily govern the SRCT/LRCT balance and emission energy, whereas narrowband emission is favored by limited overall structural and vibronic reorganization. Conversely, RISC is frequently mediated by the higher-triplet T_2/T_3 manifold rather than T_1, with Herzberg−Teller coupling strongly and selectively enhancing specific upconversion pathways. These results demonstrate that emission bandwidth cannot be predicted from LRCT character alone and that a T_1-only description is insufficient for RISC. By separating the structural origin of spectral narrowing from the vibronic basis of triplet upconversion, this work establishes mechanistic design criteria for balancing color purity and rapid RISC in hybrid MR emitters.

To establish a reliable computational methodology, we first benchmarked several density functionals against the experimental absorption and emission spectra of DBACzPh.[36] The ground- and S_1-state geometries were optimized at the B3LYP, CAM-B3LYP, M06-2X, and PBE0 levels using Gaussian 16,[48] and frequency calculations confirmed the absence of imaginary frequencies for all optimized structures, verifying them as true minima. Vibrationally resolved spectra—including absorption maxima, emission maxima, and full width at half-maximum (fwhm)—were then simulated using the thermal vibration correlation function (TVCF) formalism implemented in MOMAP.[49−54] Among the tested functionals, PBE0 delivered the most balanced agreement with the experimental spectrum of DBACzPh (Table S1) and successfully reproduced the spectral positions and bandwidths of representative related emitters (Table S2). Therefore, we adopted PBE0 for all subsequent geometry optimizations and electronic-structure analyses. All electronic-structure calculations throughout this work were performed using the polarizable continuum model (PCM) with toluene as the solvent.

With the computational methodology validated, we characterized the electronic structures of the 12 hybrid MR-TADF emitters. The dominant orbital transitions for the S_0 → S_1 excitation vary considerably across the series (ca. 46% to 98%; Table S3), indicating that a simple HOMO−LUMO

https://doi.org/10.1021/acs.jpclett.6c02618
J. Phys. Chem. Lett. 2026, 17, 11381−11390

Downloaded from pubs.acs.org/jpclcd/article-pdf/17/40/11381/6861567/6/acs.jpclett.6c02618.pdf by CHINESE UNIV OF HONG KONG SHENZHEN user on 02 November 2026

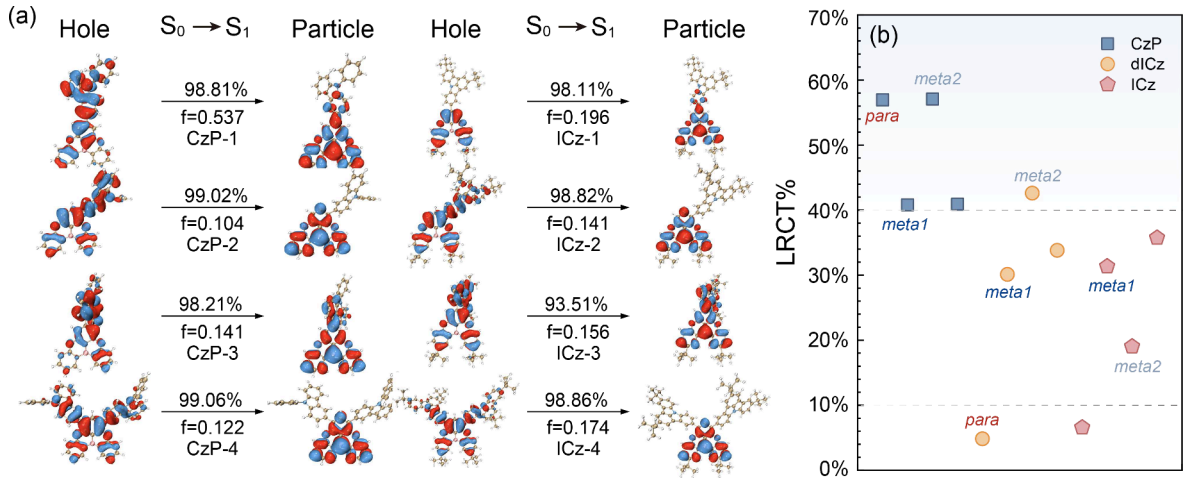


Figure 2. Charge-transfer characteristics of the hybrid MR-TADF emitters. (a) Representative hole and particle NTOs for the $S_0 \rightarrow S_1$ excitation. The percentage above each arrow is the NTO weight, and f is the oscillator strength. (b) Calculated LRCT fraction for the CzP, dICz, and ICz series and their linkage topologies. Within each series, the points from left to right correspond to para, meta1, meta2, and D−A−D connectivity.

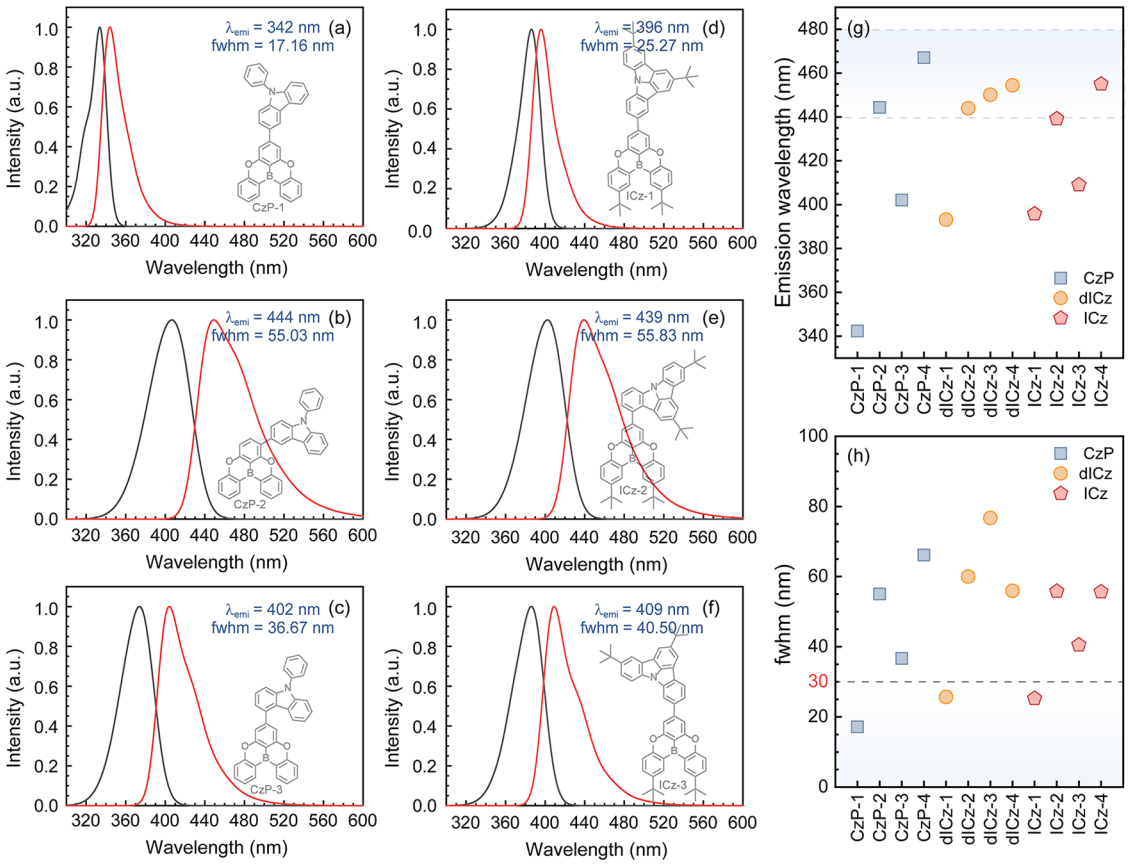


Figure 3. Calculated optical spectra and bandwidths of the hybrid MR-TADF emitters. Panels a−f show representative normalized absorption (gray) and emission (red) spectra. Panels g and h summarize the emission maxima and fwhm values, respectively, for all 12 emitters.

picture is insufficient. We therefore employed natural transition orbital (NTO) and hole−electron analyses (Section S4) to characterize the excitation character (Figure 2a and Table S4). The particle NTO is consistently localized on the BO acceptor in all 12 emitters, whereas the hole extends onto the donor to an extent that depends markedly on the molecular structure, reflecting the donor-dependent orbital composition of the excited state. Consequently, the emissive state is a hybrid of BO-centered SRCT/MR excitation and donor-to-acceptor LRCT—neither purely local nor purely charge-transfer in nature.[35,36]

The LRCT fractions, quantified through hole−electron analysis, disentangle the separate contributions of donor identity and linkage topology (Figure 2b and Table S5). The conventional CzP donor series exhibits the strongest LRCT character, with fractions ranging from 40.8% to 57.1%, stemming from the spatially separated frontier orbitals characteristic of conventional TADF donors. In marked

https://doi.org/10.1021/acs.jpclett.6c02618
J. Phys. Chem. Lett. 2026, 17, 11381−11390

Downloaded from pubs.acs.org/jpclcd/article-pdf/17/40/11381/6861567/6/acs.jpclett.6c02618.pdf by CHINESE UNIV OF HONG KONG SHENZHEN user on 02 November 2026

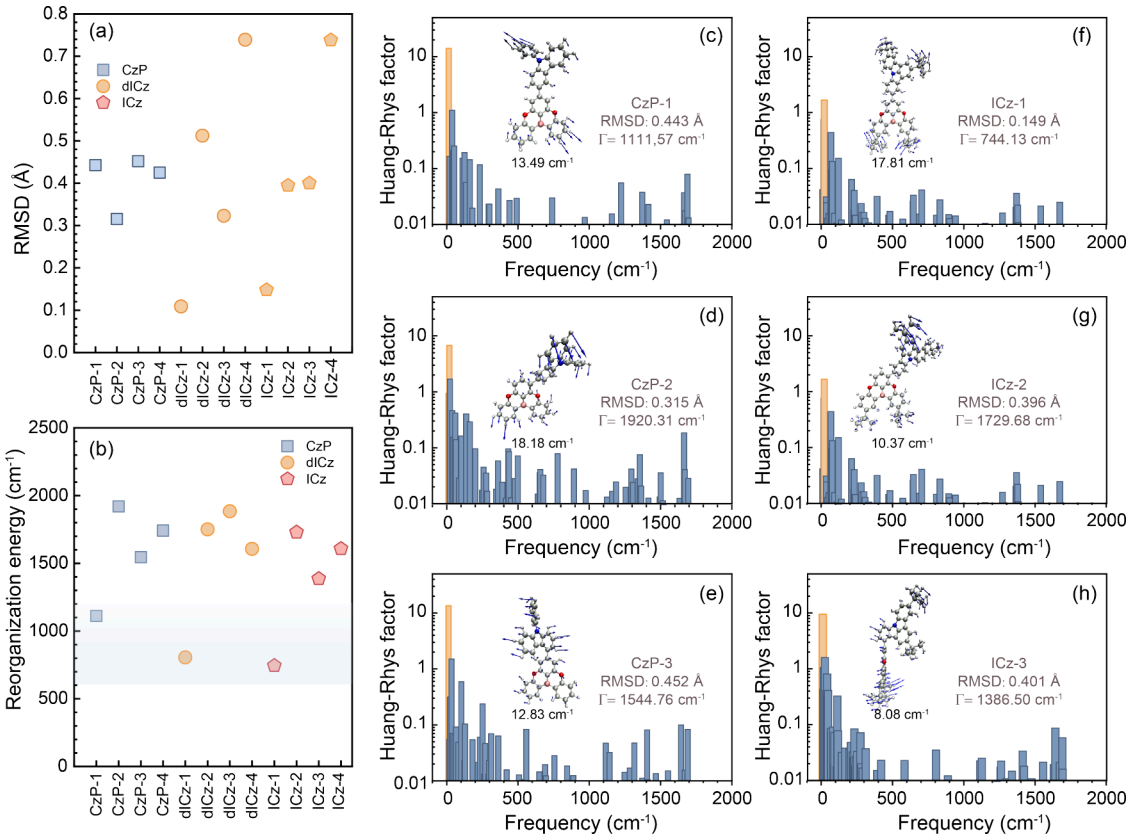


Figure 4. Geometry relaxation and vibronic coupling in the hybrid MR-TADF emitters. Panels a and b compare the root-mean-square displacement (RMSD) and reorganization energy, respectively, for all 12 emitters. Panels c–e and f–h show the mode-resolved Huang–Rhys factor distributions and displacement vectors for CzP-1–3 and ICz-1–3, respectively. Complete numerical values and mode-resolved HR distributions for all 12 emitters are provided in Table S8 and Figure S5, respectively, in the Supporting Information.

contrast, the dICz and ICz donors preserve substantially more local MR character—particularly in the para-linked analogues, dICz-1 and ICz-1, where the LRCT fractions drop to only 4.8% and 6.6%, respectively. The two meta-linked and the D–A–D analogues recover intermediate LRCT character, although the extent depends on the specific MR donor: The dICz series spans 4.8–42.6%, whereas the ICz series spans 6.6–35.7%. Thus, the label "hybrid MR" does not denote a unique electronic structure; both the donor type and its connectivity jointly determine the degree of charge-transfer admixture.[10,11,33]

This tunable electronic character is also reflected in the frontier molecular orbital energetics (Figure S1). The HOMO–LUMO gaps vary systematically across the 12 emitters, spanning from ca. 3.7 eV to ca. 4.1 eV. Within each donor series, the para-linked analogue exhibits the largest HOMO–LUMO gap, whereas the other connectivities generally show smaller gaps. The detailed ordering, however, is nonmonotonic and does not map one-to-one onto the LRCT fraction, indicating that both orbital energetics and excited-state mixing contribute to the spectral shifts examined below. These trends suggest that the molecules exhibit distinct luminescence properties, which are examined below.

The TVCF-calculated vibronic spectra of all 12 hybrid MR-TADF emitters are shown in Figure 3a–f and Figure S2. The emission wavelength depends systematically on both donor moiety and connectivity: para-linkage affords the shortest emission wavelengths (CzP-1: 342 nm; dICz-1: 393 nm; ICz-1: 396 nm), whereas meta- and D–A–D architectures lead to progressive redshifts to 402–467 nm (CzP), 444–454 nm (dICz), and 409–455 nm (ICz) (Figure 3g). This redshift correlates qualitatively with increasing LRCT fraction (Figure S3). The emission bandwidth likewise exhibits a strong connectivity dependence: para-linkage consistently yields the narrowest spectra within each donor family, with dICz-1 and ICz-1 affording fwhm values of 1663.33 and 1611.44 cm^{-1}, respectively, while the meta- and D–A–D-linked counterparts broaden markedly to 2400–3800 cm^{-1} (Figure 3h). Notably, the narrowest emission among all emitters occurs for CzP-1 (fwhm = 1467.97 cm^{-1}), which exhibits a high LRCT fraction (56.9%), comparable to that of CzP-3 (57.1%). This observation indicates that LRCT character alone does not determine spectral width, suggesting distinct physical origins for emission energy and bandwidth.

To elucidate the origin of color purity for all 12 hybrid MR-TADF emitters, we first examined the structural relaxation upon $S_0 \rightarrow S_1$ excitation. The optimized geometries (Table S6) indicate that all molecules are nonplanar due to steric congestion at the donor–acceptor junction, as characterized by the junction dihedral angle θ_1 (Table S7). Within the rigid MR-donor dICz and ICz series, the para-linked emitters undergo the smallest dihedral relaxation: 4.02° for dICz-1 and 6.54° for ICz-1, whereas the meta linkages exhibit substantially larger changes (16.99°/16.44° for dICz-2/dICz-3 and 15.95°/17.69° for ICz-2/ICz-3). Consistently, within these two series, the root-mean-square displacement (RMSD) analysis (Figure 4a and Figure S4) reveals that para-linkage most effectively suppresses structural change. Within the dICz system, dICz-1

https://doi.org/10.1021/acs.jpclett.6c02618
J. Phys. Chem. Lett. 2026, 17, 11381–11390

Downloaded from pubs.acs.org/jpclcd/article-pdf/17/40/11381/6861567/6/acs.jpclett.6c02618.pdf by CHINESE UNIV OF HONG KONG SHENZHEN user on 02 November 2026

Table 1. Calculated Vertical Singlet−Triplet Energy Gaps, Radiative Rates, Channel-Resolved RISC Rates, and Equilibrium-Limit Thermally Weighted Effective RISC Rates

		CzP-1	CzP-2	CzP-3	CzP-4	dICz-1	dICz-2
$\Delta E^{vert}_{S_1T_n}$ (eV)	S_1-T_1	0.29	0.20	0.30	0.18	0.29	0.04
	S_1-T_2	0.16	−0.09	0.13	−0.19	0.19	<0.01
	S_1-T_3	−0.10	−0.29	−0.14	−0.28	0.10	−0.06
k_r (s^{-1})		1.12×10^8	1.45×10^7	1.38×10^8	1.57×10^7	6.14×10^7	1.85×10^7
FC k_{RISC} (s^{-1})[a]	$T_1 \rightarrow S_1$	4.19×10^{-1}	1.47×10^3	1.33×10^1	1.07×10^3	5.02×10^0	1.44×10^3
	$T_2 \rightarrow S_1$	1.52×10^7	4.71×10^5	1.56×10^4	4.19×10^6	1.60×10^4	2.01×10^6
	$T_3 \rightarrow S_1$	1.90×10^6	4.90×10^6	2.51×10^6	5.39×10^5	6.14×10^3	4.61×10^5
HT-included k_{RISC} (s^{-1})	$T_1 \rightarrow S_1$	9.23×10^0	2.30×10^3	2.60×10^1	7.33×10^3	5.68×10^0	1.27×10^3
	$T_2 \rightarrow S_1$	5.21×10^7	1.38×10^6	3.28×10^4	1.47×10^7	1.35×10^7	7.17×10^6
	$T_3 \rightarrow S_1$	4.47×10^6	7.41×10^6	1.10×10^8	2.24×10^8	2.80×10^5	1.04×10^6
k^{eff}_{RISC} (s^{-1})[b]		3.60×10^5	2.33×10^3	6.50×10^1	7.34×10^3	2.27×10^5	1.36×10^6
		dICz-3	dICz-4[c]	ICz-1	ICz-2	ICz-3	ICz-4
$\Delta E^{vert}_{S_1T_n}$ (eV)	S_1-T_1	0.28	–	0.28	0.02	0.31	0.02
	S_1-T_2	0.24	–	0.17	−0.01	0.21	−0.10
	S_1-T_3	0.09	–	0.06	−0.09	0.07	−0.13
k_r (s^{-1})		1.38×10^7	2.33×10^7	6.44×10^7	2.00×10^7	1.50×10^8	2.70×10^7
FC k_{RISC} (s^{-1})[a]	$T_1 \rightarrow S_1$	1.45×10^2	–	4.71×10^{-4}	2.03×10^5	6.82×10^{-1}	5.47×10^4
	$T_2 \rightarrow S_1$	5.59×10^2	–	2.89×10^1	1.40×10^5	1.30×10^1	4.58×10^0
	$T_3 \rightarrow S_1$	6.63×10^5	–	8.28×10^6	1.92×10^6	1.14×10^5	8.93×10^3
HT-included k_{RISC} (s^{-1})	$T_1 \rightarrow S_1$	5.45×10^2	–	1.17×10^{-3}	2.95×10^5	4.69×10^0	1.14×10^5
	$T_2 \rightarrow S_1$	1.79×10^4	–	1.37×10^3	3.52×10^5	2.97×10^1	3.37×10^2
	$T_3 \rightarrow S_1$	6.40×10^5	–	3.64×10^7	4.47×10^6	1.92×10^6	1.62×10^5
k^{eff}_{RISC} (s^{-1})[b]		4.43×10^3	–	7.77×10^3	3.59×10^5	1.43×10^2	1.13×10^5

[a]The standalone FC rates are reported to quantify the channel-specific enhancement induced by Herzberg−Teller coupling. The HT−TVCF rates are used for the mechanistic analysis and for evaluating k^{eff}_{RISC}. [b]k^{eff}_{RISC} is an equilibrium-limit descriptor evaluated from the HT-included $T_1 \rightarrow S_1$, $T_2 \rightarrow S_1$, and $T_3 \rightarrow S_1$ rates using normalized Boltzmann populations according to eq 2. [c]RISC-related data for dICz-4 are unavailable because the required B2PLYP/def2-TZVP excited-state energy calculations exceeded the available local scratch storage resources. Lower-level energies were not substituted in order to maintain a consistent energetic protocol across the RISC analyses.

exhibits an RMSD of only 0.109 Å, compared with 0.512 Å for dICz-2 and 0.323 Å for dICz-3. Similarly, ICz-1 shows an RMSD of 0.149 Å, while ICz-2 and ICz-3 increase to 0.396 and 0.401 Å. The D−A−D analogues display the largest RMSD values (0.739 Å for both). These structural trends are paralleled by the reorganization energies ($\Gamma_{S1} \rightarrow S_0$; Figure 4b), which are markedly reduced for the para-linked emitters: dICz-1 and ICz-1 give values of 805.70 and 744.13 cm^{-1}, respectively, roughly half those of their meta counterparts (1750.89 cm^{-1} for dICz-2 and 1729.68 cm^{-1} for ICz-2). These results establish that para-linkage preserves the rigidity of the MR framework, minimizing both dihedral relaxation and the overall geometry change upon excitation.

Nevertheless, structural descriptors alone are insufficient to fully rationalize the observed bandwidth variations. For instance, dICz-3 exhibits a smaller RMSD (0.323 Å) than dICz-2 (0.512 Å) yet displays a substantially broader fwhm (3789.14 vs 3043.58 cm^{-1}), suggesting that vibronic coupling contributes substantially to the emission bandwidth. To elucidate these vibrational contributions, we performed Huang−Rhys (HR) factor analysis (Figure 4c−h and Figure S5). Para-linked dICz-1 and ICz-1 exhibit dominant HR factors of only 1.22 and 1.67, respectively, with negligible low-frequency activity. In contrast, meta linkages display multiple intense low-frequency modes, with dominant HR factors of 15.93 for dICz-2 and 6.89 for ICz-2, and the D−A−D analogues show exceptionally large HR factors (dICz-4:30.83; ICz-4:12.80). For the rigid MR-donor dICz and ICz series, these low-frequency modes, visualized as displacement vectors in Figure S5, correspond predominantly to donor−acceptor torsional and bending motions that are suppressed in the para-linked emitters but become more pronounced in the meta- and D−A−D-linked analogues. These distinct HR factor distributions are reflected in the spectral broadening: intense low-frequency vibronic progressions in non-para compounds give rise to extended vibrational sidebands, whereas their suppression in the para-linked emitters yields intrinsically narrow emission. Notably, the spectral width is governed not by a single promoting mode but by the collective contribution of multiple low-frequency vibrations. Although its 13.49 cm^{-1} mode has a large HR factor of 14.08 and its RMSD is 0.443 Å, CzP-1 exhibits the smallest total $S_1 \rightarrow S_0$ reorganization energy within the CzP series (1111.57 cm^{-1}) and the narrowest fwhm (1467.97 cm^{-1}). This result indicates that its narrow emission is associated with reduced overall mode-resolved vibronic reorganization rather than suppression of a single dominant low-frequency mode.

Collectively, these results are consistent with three principal observations. First, for the rigid MR-donor dICz and ICz series, para-linkage is associated with the most limited structural relaxation upon excitation, as reflected in the reduced dihedral changes, RMSD values, and reorganization energies. Second, while structural rigidity (RMSD, reorganization energy) establishes a foundation for narrow emission, the low-frequency vibronic coupling strength—as reflected in the HR factor distribution—appears to be a more direct contributor to spectral broadening than any single structural parameter alone. Third, within the rigid MR-donor series, dICz-1 and ICz-1 exhibit the narrowest fwhm values in their respective families, whereas meta- and D−A−D-linked

Downloaded from pubs.acs.org/jpclcd/article-pdf/17/40/11381/6861567/6/acs.jpclett.6c02618.pdf by CHINESE UNIV OF HONG KONG SHENZHEN user on 02 November 2026

https://doi.org/10.1021/acs.jpclett.6c02618
J. Phys. Chem. Lett. 2026, 17, 11381−11390

analogues display progressively broader spectra. In summary, these findings suggest that narrowband emission is favored by molecular designs that limit the overall structural and vibronic reorganization, with para-linkage providing an effective strategy across the present molecular series.

The reverse intersystem crossing process in these hybrid MR-TADF emitters critically depends on the excited-state energies, making the accuracy of the calculated singlet and triplet energies a prerequisite for reliable rate predictions. We found that initial attempts using adiabatic excitation energies derived from the PBE0/6-311G** optimized geometries produced appreciable errors in the state energies, which substantially compromised the subsequent kinetic evaluations. To establish a more robust computational method, we benchmarked PBE0 and nine double-hybrid functionals with the def2-TZVP basis for CzP-2 and ICz-1 and additionally evaluated B2PLYP/def2-TZVP for CzP-4 (Table S9). In addition, independent target-state-optimization density functional theory (TSO-DFT) calculations at the PBE0 level were carried out with Qbics[55] to evaluate the state ordering and energy-gap trends; however, these values exhibited poor agreement with experiment and were therefore not employed as input energies for the reported rates. Among the tested methods, B2PLYP/def2-TZVP yielded the closest agreement for CzP-2 and remained reasonably accurate for ICz-1; for the larger CzP-4 molecule, the B2PLYP value was also in good accord with experiment. Given its balanced performance across the molecules for which experimental data are available, the B2PLYP/def2-TZVP vertical excitation energies evaluated at the PBE0/6-311G**-optimized S_0 geometries were adopted to construct the singlet−triplet energy gaps used as energetic inputs for the reported RISC calculations. Both vertical and adiabatic singlet−triplet energy landscapes are summarized in Figure S6 for comparison; only the B2PLYP/def2-TZVP vertical gaps were used in the reported RISC-rate calculations. For dICz-4, the B2PLYP/def2-TZVP excited-state energy calculations could not be completed because the required local scratch storage exceeded the available computational resources. To maintain a consistent energetic protocol across the RISC analysis, the corresponding singlet−triplet gaps and channel-resolved RISC rates are not reported; lower-level results were not substituted for this molecule.

Examination of the channel-resolved rates reveals that relying solely on energy-gap criteria or static SOC matrix elements is insufficient for predicting the operative RISC pathways. Within the Franck−Condon (FC) approximation, several $T_n \rightarrow S_1$ channels remain unexpectedly slow even when the corresponding energy gaps are small (Table 1). Conversely, certain higher-triplet channels exhibit rates that far exceed the $T_1 \rightarrow S_1$ pathway, regardless of whether $\Delta E^{\mathrm{vert}}_{S_1T_1}$ is large or small. These observations indicate that neither the energy gap nor the static SOC alone can capture the full RISC network when nuclear motion modulates the electronic coupling. To address this limitation, we explicitly included Herzberg−Teller effects using the full HT-TVCF rate expression.

$$k^{\mathrm{HT}}_{f\leftarrow i} = \frac{1}{Z_i}\int d\tau_f e^{i\omega_{if}\tau_f}\left\{|H^{\mathrm{SO}}_{fi}|^2 \mathrm{Tr}[e^{-\hat{H}_f\tau_f}e^{-\hat{H}_i\tau_i}] + \sum_k 2\mathrm{Re}\left[\frac{\partial H^{\mathrm{SO}*}_{fi}}{\partial Q_{fk}}H^{\mathrm{SO}}_{fi}\right]\mathrm{Tr}[\hat{Q}_{fk}e^{-\hat{H}_f\tau_f}e^{-\hat{H}_i\tau_i}] + \sum_{kl}\frac{\partial H^{\mathrm{SO}*}_{fi}}{\partial Q_{fk}}\frac{\partial H^{\mathrm{SO}}_{fi}}{\partial Q_{fl}}\mathrm{Tr}[\hat{Q}_{fk}e^{-\hat{H}_f\tau_f}\hat{Q}_{fl}e^{-\hat{H}_i\tau_i}]\right\} \quad (1)$$

Here, i and f denote the initial triplet and final singlet states, respectively; H^{SO}_{fi} is the SOC matrix element, and Q_{fk} denotes a normal coordinate of the final-state vibrational modes. The three terms in eq 1 correspond to the FC, FC/HT interference, and HT contributions, respectively. We used the full HT−TVCF expression for the reported rates; the standalone FC values are retained in Table 1 only as a diagnostic comparison. For each spin-conversion direction, the SOC matrix element and its analytical nuclear-coordinate gradients were evaluated with PyGraSO[56] at the optimized geometry of the initial electronic state using the PBE0 electronic structures. Accordingly, the $S_1 \rightarrow T_n$ intersystem crossing (ISC) couplings were evaluated at the optimized S_1 geometry, whereas the $T_n \rightarrow S_1$ RISC couplings were evaluated separately at the corresponding optimized T_n geometries (n = 1−3); no single common geometry was used for all RISC channels. These direction- and channel-specific SOC quantities, together with the B2PLYP/def2-TZVP vertical singlet−triplet energy gaps and the optimized geometries, were supplied to the MOMAP workflow to calculate the channel-specific RISC rates. Because the B2PLYP excitation energies and PBE0 SOC quantities are evaluated at different geometries, a strict cross-method diabatic correspondence of closely spaced higher triplet states cannot be established from energy ordering alone. Accordingly, the T_2/T_3 labels are used as operational energy-order labels within the present composite protocol, and the mechanistic discussion is focused primarily on the higher-triplet manifold. To assess the sensitivity of this composite treatment to a possible interchange of the higher-triplet energetic assignments, we additionally performed a T_2/T_3 energy-reassignment test for dICz-1 by interchanging only the B2PLYP energetic inputs assigned to the two higher-triplet channels while retaining the corresponding PBE0-derived coupling quantities (Table S11). Although the absolute rates change quantitatively, the higher-triplet rate hierarchy and the pronounced channel-selective HT enhancement are preserved, supporting the robustness of the manifold-level mechanistic interpretation to this representative energetic reassignment.

The inclusion of HT coupling does not produce a uniform enhancement of the FC rates across different RISC channels. Instead, it selectively activates particular electronic-state pairs, as evident from the comparison between the FC and HT-included rates in Table 1. Within the present composite state-labeling convention, the $T_2 \rightarrow S_1$ rate of dICz-1 increases from 1.60×10^4 to 1.35×10^7 s^{-1} upon inclusion of HT coupling, corresponding to an 844-fold enhancement. For CzP-4, the $T_3 \rightarrow S_1$ rate increases from 5.39×10^5 to 2.24×10^8 s^{-1}, corresponding to a 416-fold enhancement. CzP-3 likewise shows a 44-fold enhancement to 1.10×10^8 s^{-1}. In contrast, the $T_3 \rightarrow S_1$ rate of dICz-3 remains nearly unchanged upon inclusion of HT coupling. These contrasting responses

Downloaded from pubs.acs.org/jpclcd/article-pdf/17/40/11381/6861567/6/acs.jpclett.6c02618.pdf by CHINESE UNIV OF HONG KONG SHENZHEN user on 02 November 2026

https://doi.org/10.1021/acs.jpclett.6c02618
J. Phys. Chem. Lett. 2026, 17, 11381−11390

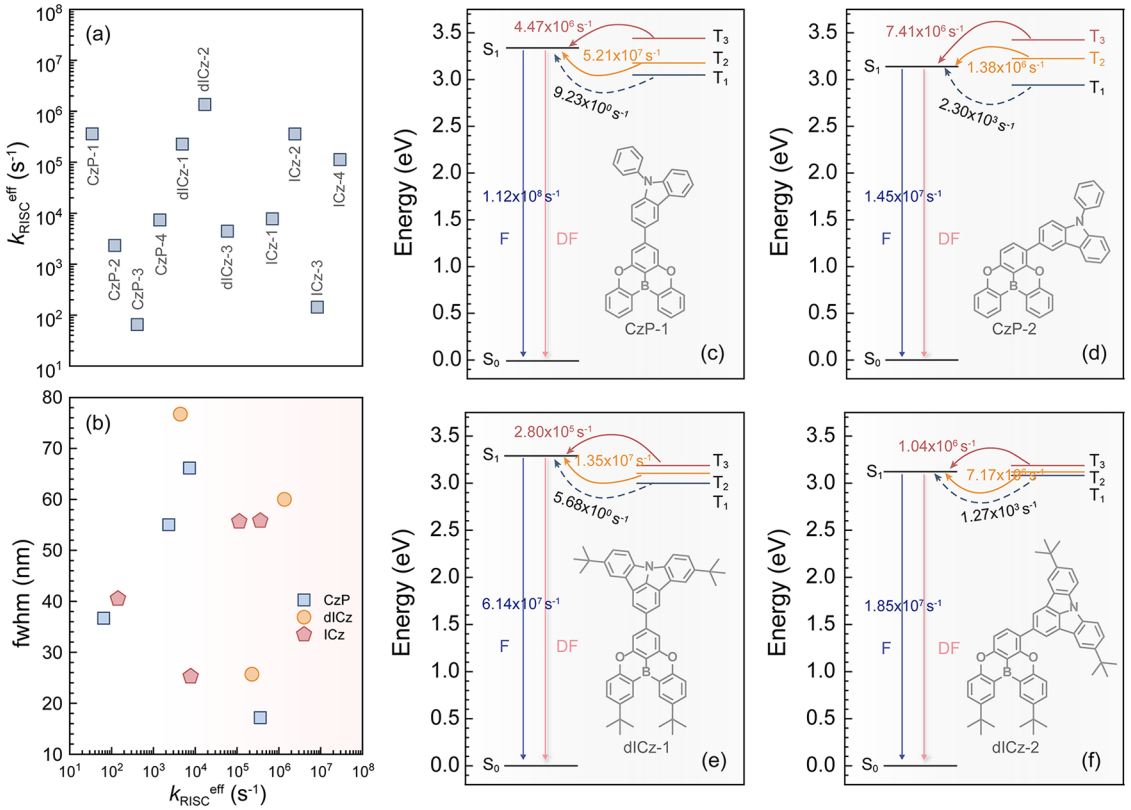


Figure 5. HT-enhanced RISC pathways and equilibrium-limit thermally weighted kinetics. (a) Equilibrium-limit thermally weighted effective RISC rates, k_{RISC}^{eff}, for the emitters with complete channel-resolved data. (b) Calculated fwhm plotted against k_{RISC}^{eff}; squares, circles, and pentagons denote the CzP, dICz, and ICz series, respectively. (c–f) B2PLYP/def2-TZVP vertical singlet–triplet energy diagrams and HT-included $T_n \rightarrow S_1$ RISC rates for CzP-1, CzP-2, dICz-1, and dICz-2, respectively. The arrows marked F and DF denote fluorescence and delayed fluorescence pathways, and all labeled rates are in s^{-1}.

demonstrate that the HT contribution is intrinsically channel-selective rather than a uniform correction to the static SOC. Although the precise T_2/T_3 assignment should be interpreted within the present state-labeling convention, the higher-triplet manifold clearly exhibits a strongly nonuniform response to nuclear-coordinate modulation of SOC.

The channel-resolved rates further demonstrate why a T_1-only description can miss kinetically important spin-conversion pathways. For CzP-1, the HT-included $T_2 \rightarrow S_1$ rate reaches 5.21×10^7 s^{-1}, whereas the $T_1 \rightarrow S_1$ rate is only 9.23 s^{-1}. Likewise, ICz-1 exhibits a $T_3 \rightarrow S_1$ rate of 3.64×10^7 s^{-1}. Across the 11 emitters with complete channel-resolved data, the fastest intrinsic RISC pathway is consistently associated with T_2 or T_3. Together with the pronounced channel-selective HT enhancements described above, these results establish that higher-triplet HT-active pathways constitute an essential component of the RISC network rather than a minor correction to the $T_1 \rightarrow S_1$ pathway. The NTO analysis (Table S4a) further reveals that the T_2/T_3 states exhibit molecule-dependent mixing between BO-centered SRCT/MR excitation and donor-to-acceptor LRCT character. Thus, the role of T_2/T_3 in RISC is not associated with a single MR or CT character but instead depends on the specific SRCT/LRCT admixture together with the state-specific energy gap and the HT-induced nuclear modulation of SOC.

The channel-resolved analysis above directly reveals the role of HT coupling in activating specific RISC pathways. To additionally compare the multistate RISC kinetics at the molecular level, we introduce an equilibrium-limit, thermally weighted effective RISC rate as a secondary descriptor. Under the limiting assumption that the T_1, T_2, and T_3 states reach Boltzmann equilibrium before spin upconversion, the HT-included channel-specific RISC rates are averaged using their normalized triplet-state populations:

$$k_{RISC}^{eff} = \frac{k_{RISC}^{T_1 \rightarrow S_1} + k_{RISC}^{T_2 \rightarrow S_1} \exp\left[-\frac{E_{T_2} - E_{T_1}}{k_B T}\right] + k_{RISC}^{T_3 \rightarrow S_1} \exp\left[-\frac{E_{T_3} - E_{T_1}}{k_B T}\right]}{1 + \exp\left[-\frac{E_{T_2} - E_{T_1}}{k_B T}\right] + \exp\left[-\frac{E_{T_3} - E_{T_1}}{k_B T}\right]} \quad (2)$$

Here, E_{T_n} denotes the B2PLYP/def2-TZVP vertical excitation energy of the nth triplet state, k_B is the Boltzmann constant, and T is the temperature (300 K). The common 3-fold spin degeneracy of the triplet states cancels upon normalization. To examine the validity of this equilibrium assumption, we additionally calculated the $T_2 \rightarrow T_1$ internal-conversion rates and estimated the reverse $T_1 \rightarrow T_2$ rates at 300 K using detailed balance (Table S10). Among the ten emitters for which both the $T_1 \rightarrow T_2$ IC and $T_1 \rightarrow S_1$ RISC rates are available, the former is faster for nine emitters. ICz-2 is the only clear exception, with $k_{IC}(T_1 \rightarrow T_2) = 1.65 \times 10^3$ s^{-1}, compared with $k_{RISC}(T_1 \rightarrow S_1) = 2.95 \times 10^5$ s^{-1}; the corresponding IC quantities are unavailable for ICz-4. Because this condition is not universal and the complete $T_1/T_2/T_3$ interconversion network was not evaluated, eq 2 is used here as an equilibrium-limit descriptor rather than as a general kinetic

https://doi.org/10.1021/acs.jpclett.6c02618
J. Phys. Chem. Lett. 2026, 17, 11381−11390

Downloaded from pubs.acs.org/jpclcd/article-pdf/17/40/11381/6861567/6/acs.jpclett.6c02618.pdf by CHINESE UNIV OF HONG KONG SHENZHEN user on 02 November 2026

model. The resulting effective rates are summarized in Figure 5a and Table 1. The corrected k_{RISC}^{eff} values span more than 4 orders of magnitude, with dICz-2 exhibiting the largest value (1.36×10^6 s^{-1}) among the emitters with complete channel-resolved data. These thermally weighted rates provide a complementary molecule-level perspective to the channel-resolved HT analysis. Specifically, a strongly HT-enhanced higher-triplet channel contributes substantially to k_{RISC}^{eff} only when the corresponding triplet state is sufficiently populated under the assumed thermal distribution. Thus, the channel-resolved FC/HT comparison identifies which RISC pathways are intrinsically activated by spin-vibronic coupling, whereas the Boltzmann weighting provides an equilibrium-limit estimate of the extent to which these pathways can contribute at the molecule level.

Figure 5b further shows that the structural requirements for narrow emission are decoupled from those for efficient triplet harvesting. dICz-2 gives the largest k_{RISC}^{eff} (1.36×10^6 s^{-1}) despite its relatively broad emission (fwhm ≈ 60 nm), whereas the narrow para-linked emitters exhibit markedly different effective rates, ranging from 7.77×10^3 s^{-1} for ICz-1 to 3.60×10^5 s^{-1} for CzP-1. This decoupling is also evident for the blue-emitting CzP-2 and ICz-2, which have comparable fwhm values of approximately 55 nm but differ in k_{RISC}^{eff} by more than 2 orders of magnitude (2.33×10^3 versus 3.59×10^5 s^{-1}). ICz-2 therefore provides the more favorable kinetic−bandwidth balance of the two. These trends indicate that connectivity-dependent structural relaxation and low-frequency vibronic coupling govern emission bandwidth, whereas the equilibrium-limit effective RISC descriptor reflects both the channel-specific HT rates and the thermal accessibility of higher triplet states. Consequently, no single linkage topology simultaneously optimizes emission bandwidth and effective RISC across the three donor families.

In summary, our calculations reveal that spectral narrowing and triplet harvesting in hybrid MR-TADF emitters are associated with distinct molecular descriptors, implying that these two performance metrics originate from different physical mechanisms. Emission bandwidth is primarily determined by structural rigidity—quantified by donor−acceptor dihedral relaxation and S_0/S_1 RMSD—and by vibronic coupling strength reflected in Huang−Rhys factors, with para-linked rigid MR donors such as dICz-1 and ICz-1 most effectively satisfying these criteria and affording fwhm below 1700 cm^{-1}. In contrast, the largest RISC rates generally arise from higher-lying T_2/T_3 channels, with HT coupling strongly and selectively enhancing specific higher-triplet pathways. This channel dependence demonstrates that nuclear modulation of SOC is essential for identifying the operative RISC pathways, while the contribution of each channel to the effective RISC rate additionally depends on its thermal accessibility. Together, these results suggest that narrowband emission and efficient triplet harvesting require complementary design strategies: suppressing structural relaxation and low-frequency vibronic coupling while promoting HT-active higher-triplet pathways. These insights provide a molecular-level framework for balancing color purity and RISC efficiency in hybrid MR-TADF emitters.

■ ASSOCIATED CONTENT

Supporting Information

The Supporting Information is available free of charge at https://pubs.acs.org/doi/10.1021/acs.jpclett.6c02618.

TVCF expressions for optical spectra and radiative and nonradiative decay rates; computational details; optical-property and singlet−triplet-gap benchmarks; vertical excitation energies and electronic transitions; natural transition orbitals, hole−electron distributions, and charge-density differences; frontier molecular orbitals and orbital energies; calculated absorption and emission spectra; optimized S_0 and S_1 geometries and selected structural parameters; geometry superpositions and RMSD analysis; emission bandwidths, reorganization energies, and mode-resolved Huang−Rhys factors; vertical and adiabatic singlet−triplet energy landscapes for RISC; $T_2 \rightarrow T_1$ internal-conversion rates, detailed-balance estimates of the reverse $T_1 \rightarrow T_2$ rates, and comparison with HT-included $T_1 \rightarrow S_1$ RISC rates; and sensitivity of the RISC rates to T_2/T_3 energetic reassignment (PDF)

■ AUTHOR INFORMATION

Corresponding Author

Zhigang Shuai − *Guangdong Basic Research Center of Excellence for Aggregate Science, School of Science and Engineering, The Chinese University of Hong Kong, Shenzhen, Guangdong 518172, People's Republic of China; MOE Key Laboratory of Organic OptoElectronics and Molecular Engineering, Department of Chemistry, Tsinghua University, 100084 Beijing, People's Republic of China;* orcid.org/0000-0003-3867-2331; Email: shuaizhigang@cuhk.edu.cn

Authors

Yaxin Wang − *Guangdong Basic Research Center of Excellence for Aggregate Science, School of Science and Engineering, The Chinese University of Hong Kong, Shenzhen, Guangdong 518172, People's Republic of China*

Xiao Chen − *MOE Key Laboratory of Organic OptoElectronics and Molecular Engineering, Department of Chemistry, Tsinghua University, 100084 Beijing, People's Republic of China;* orcid.org/0009-0004-4824-5928

Shanhao Deng − *MOE Key Laboratory of Organic OptoElectronics and Molecular Engineering, Department of Chemistry, Tsinghua University, 100084 Beijing, People's Republic of China*

Complete contact information is available at: https://pubs.acs.org/10.1021/acs.jpclett.6c02618

Notes

The authors declare no competing financial interest.

■ ACKNOWLEDGMENTS

Y.W. acknowledges support from the Young Scientists Fund of the National Natural Science Foundation of China (NSFC) (Grant No. 22503077) and the China Postdoctoral Science Foundation (Grant No. 2025M771052). This work was also supported by the National Natural Science Foundation of China (Grant Nos. T2350009 and 22433007), the Guangdong Provincial Natural Science Foundation (Grant No.

Downloaded from pubs.acs.org/jpclcd/article-pdf/17/40/11381/6861567/6/acs.jpclett.6c02618.pdf by CHINESE UNIV OF HONG KONG SHENZHEN user on 02 November 2026

2024A1515011185), and the Shenzhen City Peacock Team Project (Grant No. KQTD20240729102028011). Y.W. and Z.S. are supported by the Guangdong Basic Research Center of Excellence for Aggregate Science.

■ ABBREVIATIONS

MR	multiple resonance
TADF	thermally activated delayed fluorescence
RISC	reverse intersystem crossing
HT	Herzberg−Teller
SOC	spin−orbit coupling
TVCF	thermal vibration correlation function
OLED	organic light-emitting diode
SRCT	short-range charge transfer
LRCT	long-range charge transfer

■ REFERENCES

(1) Tang, C. W.; VanSlyke, S. A. Organic Electroluminescent Diodes. *Appl. Phys. Lett.* **1987**, *51*, 913−915.
(2) Hong, G.; Gan, X.; Leonhardt, C.; Zhang, Z.; Seibert, J.; Busch, J. M.; Bräse, S. A Brief History of OLEDs−Emitter Development and Industry Milestones. *Adv. Mater.* **2021**, *33*, 2005630.
(3) Dos Santos, J. M.; Hall, D.; Basumatary, B.; Bryden, M.; Chen, D.; Choudhary, P.; Comerford, T.; Crovini, E.; Danos, A.; De, J.; Diesing, S.; Fatahi, M.; Griffin, M.; Gupta, A. K.; Hafeez, H.; Hämmerling, L.; Hanover, E.; Haug, J.; Heil, T.; Karthik, D.; Kumar, S.; Lee, O.; Li, H.; Lucas, F.; Mackenzie, C. F. R.; Mariko, A.; Matulaitis, T.; Millward, F.; Olivier, Y.; Qi, Q.; Samuel, I. D. W.; Sharma, N.; Si, C.; Spierling, L.; Sudhakar, P.; Sun, D.; Tankelevičiutė, E.; Duarte Tonet, M.; Wang, J.; Wang, T.; Wu, S.; Xu, Y.; Zhang, L.; Zysman-Colman, E. The Golden Age of Thermally Activated Delayed Fluorescence Materials: Design and Exploitation. *Chem. Rev.* **2024**, *124*, 13736−14110.
(4) Goushi, K.; Yoshida, K.; Sato, K.; Adachi, C. Organic Light-Emitting Diodes Employing Efficient Reverse Intersystem Crossing for Triplet-to-Singlet State Conversion. *Nat. Photonics* **2012**, *6*, 253−258.
(5) Wang, Y.; Guo, Z.; Gao, Y.; Tian, Y.; Deng, Y.; Ma, X.; Yang, W. Tuning Hybridized Local and Charge-Transfer Mixing for Efficient Hot-Exciton Emission with Improved Color Purity. *J. Phys. Chem. Lett.* **2022**, *13*, 6664−6673.
(6) Dias, F. B.; Bourdakos, K. N.; Jankus, V.; Moss, K. C.; Kamtekar, K. T.; Bhalla, V.; Santos, J.; Bryce, M. R.; Monkman, A. P. Triplet Harvesting with 100% Efficiency by Way of Thermally Activated Delayed Fluorescence in Charge Transfer OLED Emitters. *Adv. Mater.* **2013**, *25*, 3707−3714.
(7) Uoyama, H.; Goushi, K.; Shizu, K.; Nomura, H.; Adachi, C. Highly Efficient Organic Light-Emitting Diodes from Delayed Fluorescence. *Nature* **2012**, *492*, 234−238.
(8) Zhang, Q.; Li, B.; Huang, S.; Nomura, H.; Tanaka, H.; Adachi, C. Efficient Blue Organic Light-Emitting Diodes Employing Thermally Activated Delayed Fluorescence. *Nat. Photonics* **2014**, *8*, 326−332.
(9) Qiu, X.; Tian, G.; Lin, C.; Pan, Y.; Ye, X.; Wang, B.; Ma, D.; Hu, D.; Luo, Y.; Ma, Y. Narrowband Emission from Organic Fluorescent Emitters with Dominant Low-Frequency Vibronic Coupling. *Adv. Opt. Mater.* **2021**, *9*, 2001845.
(10) Huang, J.-W.; Hsu, Y.-C.; Wu, X.; Wang, S.; Gan, X.-Q.; Zheng, W.-Q.; Zhang, H.; Gong, Y.-Z.; Hung, W.-Y.; Chou, P.-T.; Zhu, W. Influence of Charge Transfer Strength on Emission Bandwidth for Multiple-Resonance Emitters via Systematically Tuning the Acceptor-Donor Assembly. *J. Mater. Chem. C* **2022**, *10*, 7866−7874.
(11) Huang, F.; Fan, X.-C.; Cheng, Y.-C.; Wu, H.; Shi, Y.-Z.; Yu, J.; Wang, K.; Lee, C.-S.; Zhang, X.-H. Distinguishing the Respective Determining Factors for Spectral Broadening and Concentration Quenching in Multiple Resonance Type TADF Emitter Systems. *Mater. Horiz.* **2022**, *9*, 2226−2232.
(12) Hatakeyama, T.; Shiren, K.; Nakajima, K.; Nomura, S.; Nakatsuka, S.; Kinoshita, K.; Ni, J.; Ono, Y.; Ikuta, T. Ultrapure Blue Thermally Activated Delayed Fluorescence Molecules: Efficient HOMO-LUMO Separation by the Multiple Resonance Effect. *Adv. Mater.* **2016**, *28*, 2777−2781.
(13) Kondo, Y.; Yoshiura, K.; Kitera, S.; Nishi, H.; Oda, S.; Gotoh, H.; Sasada, Y.; Yanai, M.; Hatakeyama, T. Narrowband Deep-Blue Organic Light-Emitting Diode Featuring an Organoboron-Based Emitter. *Nat. Photonics* **2019**, *13*, 678−682.
(14) Wang, Y.; Tian, Y.; Gao, Y.; Guo, Z.; Xue, Z.; Han, Y.; Yang, W.; Ma, X. Resolving the Photophysics of Nitrogen-Embedded Multiple Resonance Emitters: Origin of Color Purity and Emitting Efficiency. *J. Phys. Chem. Lett.* **2023**, *14*, 9665−9676.
(15) Liu, T.; Cheng, C.; Lou, W.; Deng, C.; Liu, J.; Wang, D.; Tsuboi, T.; Zhang, Q. Ultrapure Blue Organic Light-Emitting Diodes Exhibiting 13 nm Full Width at Half-Maximum. *J. Mater. Chem. C* **2022**, *10*, 7799−7802.
(16) Zeng, X.; Wang, X.; Zhang, Y.; Meng, G.; Wei, J.; Liu, Z.; Jia, X.; Li, G.; Duan, L.; Zhang, D. Nitrogen-Embedded Multi-Resonance Heteroaromatics with Prolonged Homogeneous Hexatomic Rings. *Angew. Chem., Int. Ed.* **2022**, *61*, e202117181.
(17) Lee, H. L.; Jeon, S. O.; Kim, I.; Kim, S. C.; Lim, J.; Kim, J.; Park, S.; Chwae, J.; Son, W.-J.; Choi, H.; Lee, J. Y. Multiple-Resonance Extension and Spin-Vibronic-Coupling-Based Narrowband Blue Organic Fluorescence Emitters with Over 30% Quantum Efficiency. *Adv. Mater.* **2022**, *34*, 2202464.
(18) Hirai, H.; Nakajima, K.; Nakatsuka, S.; Shiren, K.; Ni, J.; Nomura, S.; Ikuta, T.; Hatakeyama, T. One-Step Borylation of 1,3-Diaryloxybenzenes Towards Efficient Materials for Organic Light-Emitting Diodes. *Angew. Chem., Int. Ed.* **2015**, *54*, 13581−13585.
(19) Chen, F.; Zhao, L.; Wang, X.; Yang, Q.; Li, W.; Tian, H.; Shao, S.; Wang, L.; Jing, X.; Wang, F. Novel Boron- and Sulfur-Doped Polycyclic Aromatic Hydrocarbon as Multiple Resonance Emitter for Ultrapure Blue Thermally Activated Delayed Fluorescence Polymers. *Sci. China: Chem.* **2021**, *64*, 547−551.
(20) Yuan, Y.; Tang, X.; Du, X.-Y.; Hu, Y.; Yu, Y.-J.; Jiang, Z.-Q.; Liao, L.-S.; Lee, S.-T. The Design of Fused Amine/Carbonyl System for Efficient Thermally Activated Delayed Fluorescence: Novel Multiple Resonance Core and Electron Acceptor. *Adv. Opt. Mater.* **2019**, *7*, 1801536.
(21) Kang, J.; Lee, H. L.; Jeon, S. O.; Bae, H. J.; Kim, S. C.; Han, S.; Lee, J. Y. Spin-Flip-Restricted Multiple-Resonance Emitters for Extended Device Lifetime in Indolocarbazole-Based Blue Organic Light-Emitting Diodes. *Adv. Sci. (Weinheim, Ger.)* **2024**, *11*, 2405604.
(22) Keruckiene, R.; Vaitusionak, A. A.; Hulnik, M. I.; Berezianko, I. A.; Gudeika, D.; Macionis, S.; Mahmoudi, M.; Volyniuk, D.; Valverde, D.; Olivier, Y.; Woon, K. L.; Kostjuk, S. V.; Reineke, S.; Grazulevicius, J. V.; Sini, G. Is a Small Singlet-Triplet Energy Gap a Guarantee of TADF Performance in MR-TADF Compounds? Impact of the Triplet Manifold Energy Splitting. *J. Mater. Chem. C* **2024**, *12*, 3450−3464.
(23) Hall, D.; Sancho-García, J. C.; Pershin, A.; Ricci, G.; Beljonne, D.; Zysman-Colman, E.; Olivier, Y. Modeling of Multiresonant Thermally Activated Delayed Fluorescence Emitters−Properly Accounting for Electron Correlation Is Key! *J. Chem. Theory Comput.* **2022**, *18*, 4903−4918.
(24) Situ, Z.; Li, X.; Gao, H.; Zhang, J.; Li, Y.; Zhao, F.; Kong, J.; Zhao, H.; Zhou, M.; Wang, Y.; Kuang, Z.; Xia, A. Accelerating Intersystem Crossing in Multiresonance Thermally Activated Delayed Fluorescence Emitters via Long-Range Charge Transfer. *J. Phys. Chem. Lett.* **2024**, *15*, 4197−4205.
(25) Huang, Z.; Xie, H.; Miao, J.; Wei, Y.; Zou, Y.; Hua, T.; Cao, X.; Yang, C. Charge Transfer Excited State Promoted Multiple Resonance Delayed Fluorescence Emitter for High-Performance Narrowband Electroluminescence. *J. Am. Chem. Soc.* **2023**, *145*, 12550−12560.
(26) Moon, J.; Han, S.; Lee, J. Y. Hybrid Multi-Resonance Thermally Activated Delayed Fluorescent Emitters with High Efficiency and High Color Purity. *Adv. Opt. Mater.* **2025**, *13*, 2402214.

Downloaded from pubs.acs.org/jpclcd/article-pdf/17/40/11381/6861567/6/acs.jpclett.6c02618.pdf by CHINESE UNIV OF HONG KONG SHENZHEN user on 02 November 2026

https://doi.org/10.1021/acs.jpclett.6c02618
J. Phys. Chem. Lett. 2026, 17, 11381−11390

(27) Li, P.; Zhang, Y.; Lv, Q.; Sun, C.; Li, W.; Zhou, C.; Chen, R. Manipulating Multiple Resonance-Charge Transfer Hybrid Proportion for Developing Red Narrowband Thermally Activated Delayed Fluorescence Materials. *J. Phys. Chem. Lett.* **2023**, *14*, 8531−8540.
(28) Lee, H. L.; Kang, J.; Lim, J.; Kim, S. C.; Jeon, S. O.; Lee, J. Y. Hybridization of Short-Range and Long-Range Charge Transfer Excited States in Multiple Resonance Emitter. *Nat. Commun.* **2023**, *14*, 4818.
(29) Huang, X.; Xu, Y.; Miao, J.; Jing, Y.-Y.; Wang, S.; Ye, Z.; Huang, Z.; Cao, X.; Yang, C. Donor-Modified Multiple Resonance Emitters with Accelerated Reverse Intersystem Crossing towards High-Efficiency and Narrowband Deep-Blue OLEDs. *J. Mater. Chem. C* **2023**, *11*, 11885−11894.
(30) Chen, G.; Wang, J.; Chen, W.-C.; Gong, Y.; Zhuang, N.; Liang, H.; Xing, L.; Liu, Y.; Ji, S.; Zhang, H.-L.; Zhao, Z.; Huo, Y.; Tang, B. Z. Triphenylamine-Functionalized Multiple-Resonance TADF Emitters with Accelerated Reverse Intersystem Crossing and Aggregation-Induced Emission Enhancement for Narrowband OLEDs. *Adv. Funct. Mater.* **2023**, *33*, 2211893.
(31) Luo, X.-F.; Shen, L.; Wang, J.-Y.; Xiao, X. Double Charge Transfer Processes Enable a Green Multiple Resonance-Induced Thermally Activated Delayed Fluorescence Emitter for an Efficient Narrowband OLED. *Chem. Commun.* **2024**, *60*, 574−577.
(32) Meng, Y.; Chen, G.; Peng, H.; Miao, J.; Liu, H.; Yang, C. Hybridization of Long-Range and Short-Range Charger Transfer Enables Efficient Thermally Activated Delayed Fluorescent and Hyperfluorescent OLEDs. *Adv. Opt. Mater.* **2024**, *12*, 2401479.
(33) Fan, X.-C.; Wang, K.; Shi, Y.-Z.; Chen, J.-X.; Huang, F.; Wang, H.; Hu, Y.-N.; Tsuchiya, Y.; Ou, X.-M.; Yu, J.; Adachi, C.; Zhang, X.-H. Managing Intersegmental Charge-Transfer and Multiple Resonance Alignments of D_3-A Typed TADF Emitters for Red OLEDs with Improved Efficiency and Color Purity. *Adv. Opt. Mater.* **2022**, *10*, 2101789.
(34) Zou, Y.; Yu, M.; Xu, Y.; Xiao, Z.; Song, X.; Hu, Y.; Xu, Z.; Zhong, C.; He, J.; Cao, X.; Li, K.; Miao, J.; Yang, C. Acceleration of Reverse Intersystem Crossing in Multi-Resonance TADF Emitter. *Chem.* **2024**, *10*, 1485−1501.
(35) Jiang, K.; Chang, X.; Zhu, J.; Zhu, T.; Yu, J.; Wang, Y.; Zhang, Y.; Ma, D.; Zhu, W. High-Performance Solution-Processable Organic Light-Emitting Diode Based on a Narrowband Near-Ultraviolet Emitter and a Hot Exciton Strategy. *Angew. Chem., Int. Ed.* **2025**, *64*, e202421520.
(36) Barman, D.; Tsuchiya, Y.; Adachi, C. Horizontally Oriented MRCT-Type TADF Emitter Achieving EQE over 40% for Sky-Blue OLED. *Nat. Commun.* **2025**, *16*, 5023.
(37) Wang, Y.; Shuai, Z. Theoretical Design of Heavy-Atom Embedded ICz-Based Multi-Resonance TADF Emitters with High Efficiency and Narrow Emission Width. *J. Phys. Chem. Lett.* **2025**, *16*, 7752−7762.
(38) Peng, Q.; Fan, D.; Duan, R.; Yi, Y.; Niu, Y.; Wang, D.; Shuai, Z. Theoretical Study of Conversion and Decay Processes of Excited Triplet and Singlet States in a Thermally Activated Delayed Fluorescence Molecule. *J. Phys. Chem. C* **2017**, *121*, 13448−13456.
(39) T. do Casal, M.; Badawy, Y.; Escudero, D. Modeling MR-TADF Emitters: Excited-State Decay Rate Constants and Wave Function Descriptors. *J. Phys. Chem. C* **2024**, *128*, 18170−18181.
(40) Karak, P.; Adhikary, R.; Chakrabarti, S. Nonradiative Spin-Forbidden Decay Processes in π- and Multiresonance-Acceptor-Based TADF Molecules. *J. Phys. Chem. C* **2024**, *128*, 16879−16891.
(41) Sanyam; Khatua, R.; Mondal, A. Cost-Effective Approach for Modeling of Multiresonant Thermally Activated Delayed Fluorescence Emitters. *J. Chem. Theory Comput.* **2023**, *19*, 9290−9301.
(42) Gibson, J.; Monkman, A. P.; Penfold, T. J. The Importance of Vibronic Coupling for Efficient Reverse Intersystem Crossing in Thermally Activated Delayed Fluorescence Molecules. *ChemPhysChem* **2016**, *17*, 2956−2961.
(43) Etherington, M. K.; Gibson, J.; Higginbotham, H. F.; Penfold, T. J.; Monkman, A. P. Revealing the Spin-Vibronic Coupling Mechanism of Thermally Activated Delayed Fluorescence. *Nat. Commun.* **2016**, *7*, 13680.
(44) Lin, S.; Pei, Z.; Zhang, B.; Ma, H.; Liang, W. Vibronic Coupling Effect on the Vibrationally Resolved Electronic Spectra and Intersystem Crossing Rates of a TADF Emitter: 7-PhQAD. *J. Phys. Chem. A* **2022**, *126*, 239−248.
(45) Karak, P.; Ruud, K.; Chakrabarti, S. Spin-Vibronic Interaction Induced Reverse Intersystem Crossing: A Case Study with TXO-TPA and TXO-PhCz Molecules. *J. Chem. Phys.* **2022**, *157*, 174101.
(46) Mariano, L. A.; Mondal, S.; Lunghi, A. Spin-Vibronic Dynamics in Open-Shell Systems beyond the Spin Hamiltonian Formalism. *J. Chem. Theory Comput.* **2024**, *20*, 323−332.
(47) Chen, X.; Sun, L.; Sukhanov, A. A.; Doria, S.; Bussotti, L.; Zhao, J.; Xu, H.; Dick, B.; Voronkova, V. K.; Di Donato, M. Photophysics and Photochemistry of Thermally Activated Delayed Fluorescence Emitters Based on the Multiple Resonance Effect: Transient Optical and Electron Paramagnetic Resonance Studies. *Chem. Sci.* **2024**, *15*, 10867−10881.
(48) Frisch, M. J.; Trucks, G. W.; Schlegel, H. B.; Scuseria, G. E.; Robb, M. A.; Cheeseman, J. R.; Scalmani, G.; Barone, V.; Petersson, G. A.; Nakatsuji, H.; Li, X.; Caricato, M.; Marenich, A. V.; Bloino, J.; Janesko, B. G.; Gomperts, R.; Mennucci, B.; Hratchian, H. P.; Ortiz, J. V.; Izmaylov, A. F.; Sonnenberg, J. L.; Williams-Young, D.; Ding, F.; Lipparini, F.; Egidi, F.; Goings, J.; Peng, B.; Petrone, A.; Henderson, T.; Ranasinghe, D.; Zakrzewski, V. G.; Gao, J.; Rega, N.; Zheng, G.; Liang, W.; Hada, M.; Ehara, M.; Toyota, K.; Fukuda, R.; Hasegawa, J.; Ishida, M.; Nakajima, T.; Honda, Y.; Kitao, O.; Nakai, H.; Vreven, T.; Throssell, K.; Montgomery, J. A., Jr.; Peralta, J. E.; Ogliaro, F.; Bearpark, M. J.; Heyd, J. J.; Brothers, E. N.; Kudin, K. N.; Staroverov, V. N.; Keith, T. A.; Kobayashi, R.; Normand, J.; Raghavachari, K.; Rendell, A. P.; Burant, J. C.; Iyengar, S. S.; Tomasi, J.; Cossi, M.; Millam, J. M.; Klene, M.; Adamo, C.; Cammi, R.; Ochterski, J. W.; Martin, R. L.; Morokuma, K.; Farkas, O.; Foresman, J. B.; Fox, D. J. *Gaussian 16, Revision A.03*; Gaussian, Inc.: Wallingford, CT, 2016.
(49) Niu, Y.; Li, W.; Peng, Q.; Geng, H.; Yi, Y.; Wang, L.; Nan, G.; Wang, D.; Shuai, Z. MOlecular MAterials Property Prediction Package (MOMAP) 1.0: A Software Package for Predicting the Luminescent Properties and Mobility of Organic Functional Materials. *Mol. Phys.* **2018**, *116*, 1078−1090.
(50) Shuai, Z. Thermal Vibration Correlation Function Formalism for Molecular Excited State Decay Rates. *Chin. J. Chem.* **2020**, *38*, 1223−1232.
(51) Peng, Q.; Yi, Y.; Shuai, Z.; Shao, J. Toward Quantitative Prediction of Molecular Fluorescence Quantum Efficiency: Role of Duschinsky Rotation. *J. Am. Chem. Soc.* **2007**, *129*, 9333−9339.
(52) Niu, Y.; Peng, Q.; Shuai, Z. Promoting-Mode Free Formalism for Excited State Radiationless Decay Process with Duschinsky Rotation Effect. *Sci. China, Ser. B: Chem.* **2008**, *51*, 1153−1158.
(53) Peng, Q.; Yi, Y.; Shuai, Z.; Shao, J. Excited State Radiationless Decay Process with Duschinsky Rotation Effect: Formalism and Implementation. *J. Chem. Phys.* **2007**, *126*, 114302.
(54) Niu, Y.; Peng, Q.; Deng, C.; Gao, X.; Shuai, Z. Theory of Excited State Decays and Optical Spectra: Application to Polyatomic Molecules. *J. Phys. Chem. A* **2010**, *114*, 7817−7831.
(55) Zhang, J.; Tang, Z.; Zhang, X.; Zhu, H.; Zhao, R.; Lu, Y.; Gao, J. Target State Optimized Density Functional Theory for Electronic Excited and Diabatic States. *J. Chem. Theory Comput.* **2023**, *19*, 1777−1789.
(56) Hagai, M.; Fujimoto, K. J.; Yanai, T. PyGraSO: Analytical Nuclear Derivatives of Spin-Orbit Coupling for Intersystem Crossing Dynamics Simulations. *J. Chem. Theory Comput.* **2025**, *21*, 11604−11619.

Downloaded from pubs.acs.org/jpclcd/article-pdf/17/40/11381/6861567/6/acs.jpclett.6c02618.pdf by CHINESE UNIV OF HONG KONG SHENZHEN user on 02 November 2026

https://doi.org/10.1021/acs.jpclett.6c02618
J. Phys. Chem. Lett. 2026, 17, 11381−11390